Available online at www.sciencedirect.com
SCIENCE DIRECT
Polymer 47 (2006) 2389–2401
polymer
www.elsevier.com/locate/polymer

The influence of matrix modification on fracture mechanisms in rubber toughened polymethylmethacrylate

Laure Lalande [a], Christopher J.G. Plummer [a], Jan-Anders E. Månson [a,*], Pierre Gérard [b]

[a] *Laboratoire de Technologie de Composites et Polymères (LTC), IMX-STI, Ecole Polytechnique Fédérale de Lausanne (EPFL), CH-1015 Lausanne, Switzerland*
[b] *Groupement de Recherche de Lacq, Arkema, R.N. 17. B.P. 34, F-64170 Lacq, France*

Received 16 November 2005; received in revised form 30 January 2006; accepted 3 February 2006

Abstract

The fracture behavior of composite rubber particle-toughened polymethylmethacrylate has been investigated over a wide range of test speeds, encompassing impact conditions. When the entanglement density of the matrix was increased and its glass transition temperature reduced by copolymerization, there were significant increases in the crack initiation and propagation resistance of the particle-toughened materials at low to intermediate speeds. At impact speeds, on the other hand, where crazing became the dominant matrix microdeformation mechanism in all the materials investigated, the fracture response of the copolymer matrix was closer to that of the polymethylmethacrylate homopolymer, and the toughening effect of the rubber particles was no longer effective in either case. This is discussed in terms of the onset of the matrix β transition, associated with the transition from shear to crazing, and the α transition of the rubber domains, both of which occurred in the temperature range immediately below room temperature in low frequency dynamic torsion measurements.

Keywords: High speed testing; Polymer fracture; PMMA

1. Introduction

Polymethylmethacrylate (PMMA) is a glassy amorphous polymer with excellent optical properties and long-term stability in comparison with relatively tough transparent polymers, such as polycarbonate (PC). However, PMMA has the disadvantage of poor impact toughness, which makes it unsuitable for many engineering purposes. To broaden the range of application of PMMA, various strategies may be envisaged. One approach consists of adding well dispersed rubber particles to the matrix (or, as in the present case, composite core/shell rubber particles [1]). Given a suitable choice of particle size and the chemical composition, this can lead to substantial improvements in impact resistance without significantly compromising the optical properties [2,3]. A second approach is to improve the mechanical behavior of the matrix by altering its chemical characteristics, for example, by introduction of a suitable comonomer during synthesis [4]. A third approach, which will be explored here, is to exploit the potentially cumulative effects of combined rubber toughening and matrix modification on the overall toughness.

The intrinsic rate sensitivity of polymer mechanical properties makes it important to develop characterization techniques that cover the full range of loading rates likely to be encountered in practice, including those associated with impact. Indeed, given that most polymers tend to undergo a ductile-brittle transition as the loading rate is increased, an understanding of the rate dependence of the competition between the different microdeformation mechanisms associated with such transitions (cavitation, crazing, homogeneous shear), and how it is influenced by the properties of the matrix and the particles, is important for interpretation and the rational development of impact resistant materials [5]. In the present work, fracture mechanics-based tensile and compact tension tests on bulk specimens of modified PMMA over a wide range of test speeds have, therefore, been combined with studies of the associated microdeformation mechanisms, based on: (i) scanning electron microscopy (SEM) and transmission electron microscopy (TEM) observations of the crack tip damage mechanisms in bulk specimens [6–10]; (ii) low-dose TEM studies of microdeformation in thin electron transparent films deformed over a comparable range of test speeds, using the copper grid technique [11]. The aim has been to establish a link

* Corresponding author. Tel.: +41 21 693 4285; fax: +41 21 693 5880.
E-mail address: jan-anders.manson@epfl.ch (J.-A.E. Månson).

0032-3861/$ - see front matter © 2006 Elsevier Ltd. All rights reserved.
doi:10.1016/j.polymer.2006.02.016

between the observed microdeformation mechanisms and the global mechanical behavior, and hence explore the potential for synergy between matrix modification and rubber toughening in the fracture response.

2. Experimental

2.1. Materials

The matrices chosen for study were PMMA-based copolymers, supplied by Atoglas (Arkema). They are listed in Table 1, along with the corresponding values of the glass transition temperature, T_g, measured by differential scanning calorimetry heating scans at 10 K/min, the weight average molar mass, M_w, measured by gel permeation chromatography and the entanglement molar mass, M_e, estimated from the rubbery plateau modulus in dynamic mechanical analysis temperature sweeps at 1 Hz [12]. The polymer referred to as V825-LC in Table 1 was essentially a PMMA homopolymer that contained residual amounts of an acrylic-based comonomer, whose role is generally to stabilize the polymer chains with respect to unzipping reactions provoked by chemical degradation. However, in V825-HC the proportion of comonomer was significantly increased, resulting in the property changes indicated in Table 1. V825-LC and V825-HC and the corresponding rubber toughened grades provide the focus in what follows, although reference will also be made to intermediate matrix compositions in the discussion.

The composite core/shell rubber particles were also supplied by Atoglas. The basic particle morphology (Fig. 1) was obtained by emulsion polymerization, giving a glassy PMMA-rich core surrounded by an inner rubbery shell and an outer grafted PMMA shell, whose purpose was to ensure good adhesion with the matrix. The overall diameter of the particles referred to here as 3LA was approximately 250 nm. Two further types of particle, 3LB and 3LC, were also investigated in order to confirm or otherwise the generality of the observations made with the 3LA particles. They were produced in the same way as 3LA, but the rubbery shell was relatively lightly cross linked in the 3LB particles, and somewhat thicker in the 3LC particles. The two different matrices were combined with 47 wt% particles in the form of 70×100 mm^2 injection molded plaques.

2.2. Mechanical characterization

Simple tensile tests were performed at 10^{-4}, 10^{-3} and 5×10^{-3} m/s at room temperature using a screw driven tensile test machine (UTS Testsysteme GmbH) and the specimen geometry illustrated in Fig. 2(a) (thickness 4 mm). Overall stresses and strains were calculated according to the following definitions:

$$\sigma = \frac{F}{S} = \frac{FL}{S_0L_0} = F\frac{L_0+\Delta L}{S_0L_0}$$
and
$$\varepsilon = \int_{L_0}^{L}\frac{\mathrm{d}l}{l} = [\ln(l)]_{L_0}^{L} = \ln\left(\frac{L}{L_0}\right) = \ln\left(\frac{L_0+\Delta L}{L_0}\right) \quad (1)$$

where F is the force, L is the specimen gage length, L_0 is the initial gage length (about 15 mm), S is the cross-section and S_0 is the initial cross-section. In ductile specimens, which showed a clear yield drop, the yield stress, σ_y, was taken to correspond to the first maximum in the stress strain curve.

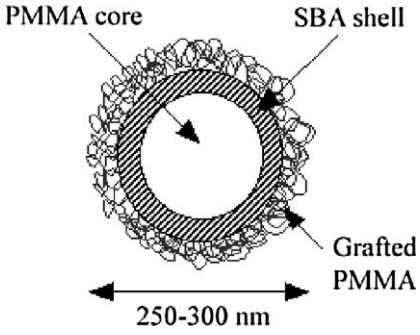

Fig. 1. Schematic of the basic composite core/shell rubber particle geometry.

To characterize the crack initiation and propagation behavior, tensile tests were carried out on notched compact tension (CT) specimens (Fig. 2(b)) using a Schenck Hydropuls POZ1152 servo-hydraulic apparatus. Force–displacement curves were obtained at room temperature (RT) at speeds from roughly 10^{-4} to 9 m/s. Each material was tested at least three times at each speed, and the data given in what follows correspond to average values for the three tests. A maximum stress intensity factor, K_{max}, was determined from

$$K_{max} = f\left(\frac{a}{W}\right)\frac{F_{max}}{B\sqrt{W}} \quad (2)$$

where F_{max} is the force maximum in the tensile test, a is the crack length, B is the thickness of the specimen and W is its width (Fig. 2(b)). $f(a/W)$ is given by

$$f = \frac{2+(a/W)}{(1-(a/W))^{3/2}}\left[0.886+4.64\left(\frac{a}{W}\right)-13.32\left(\frac{a}{W}\right)^2 +14.72\left(\frac{a}{W}\right)^3-5.60\left(\frac{a}{W}\right)^4\right] \quad (3)$$

for the geometry in Fig. 2(b) [5]. K_{max} is equivalent to the mode I critical stress intensity factor for crack initiation, K_{IC} when the strict conditions for linear elastic fracture mechanics (LEFM) testing are met, in which case the following criteria should be fulfilled [13]:

$$B,a,W-a \geq 2.5\left(\frac{K_{IC}}{\sigma_y}\right)^2 \quad (4)$$

Table 1
Characteristics of the matrix materials

	M_w (g/mol)	M_e (g/mol)	T_g (K)	Bending modulus (GPa)
V825-LC	93,000	10,242	385	3.4
V825-HC	159,510	5023	337	2.8

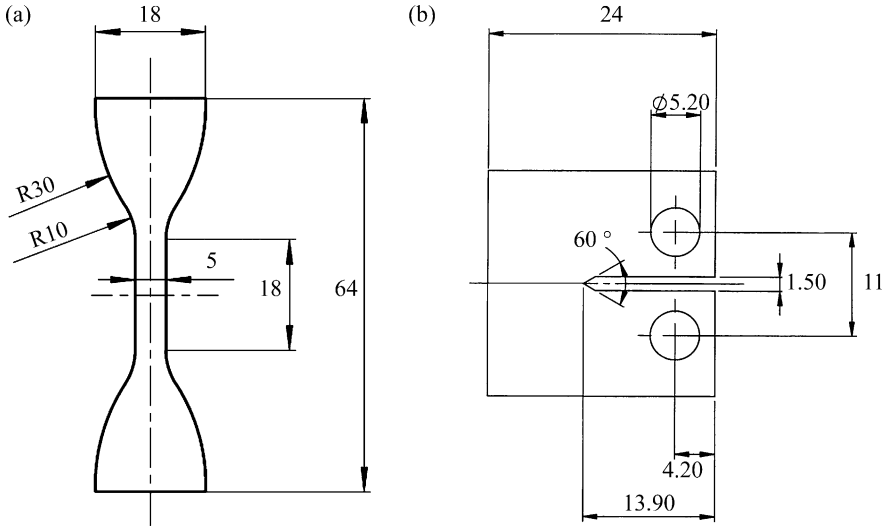

Fig. 2. Specimen geometries for (a) simple tensile tests and (b) fracture tests (lengths in millimeters).

In the present case, deviations from LEFM conditions were apparent at relatively low speeds, and transient acceleration at high speeds also led to spurious curvature of the force–displacement curves at small deformations. This was in part due to the use of a damping system to eliminate dynamic effects at test speeds greater than about 0.1 m/s, and hence maintain quasi-static conditions up to the highest speeds investigated [14]. The results are, therefore, given in terms of K_{max} rather than K_{IC}. Although K_{max} cannot necessarily be considered an intrinsic materials parameter, its providing a conservative estimate of K_{IC} when LEFM conditions are not met, it remains a useful quantity for comparing the crack initiation behavior of the different materials and their behavior under different conditions, particularly if, as in the present case, a single test geometry and test method are employed over the whole range of test speeds of interest [15]. An approximate measure of the crack propagation energy, U_{prop}, and hence an indication of the crack propagation mode, was provided by the area under the force–displacement curve for $F > F_{max}$, as shown schematically in Fig. 3.

2.3. Morphological characterization

Two basic techniques were used for morphological characterization:

1. Post mortem sectioning from the crack tip region in bulk compact tensile (CT) specimens for scanning electron microscopy (SEM; Philips XL30 equipped with a field emission gun) or transmission electron microscopy (TEM; Philips CM20 operated at 200 kV) [7].
2. Deformation and TEM observation of thin sections taken from the bulk specimens, using the copper grid technique [11].

TEM micrographs of 100 nm thick ultramicrotomed sections (Reichert-Jung Ultracut E/Diatome 35° diamond knife) taken from undeformed RuO_4-stained [6,7,16–18] specimens containing the different types of particle and mounted on carbon/colloidon covered copper grids are shown in Fig. 4(a) and (b). In each case, the most heavily stained (darkest) regions correspond to the rubbery phase. The outer grafted layer of PMMA was indistinguishable from the matrix, but the proportions of the core and rubbery shell estimated from the micrographs were in approximate agreement with the values given by the supplier. It should nevertheless be borne in mind that the observations were derived from sections taken at arbitrary positions with respect to those of the particles, so that the images of these latter did not necessarily correspond to diametric sections. Staining of the microtomed surfaces with RuO_4, followed by gold coating to prevent charging, again resulted in pronounced contrast between the rubbery layers of the particles and the surrounding glassy material in the SEM, as shown in Fig. 4(d). The main interest of SEM for the observation of bulk specimens, apart from the relatively straightforward specimen preparation, is that it can provide both local detail and an overview of the damage zone (in TEM,

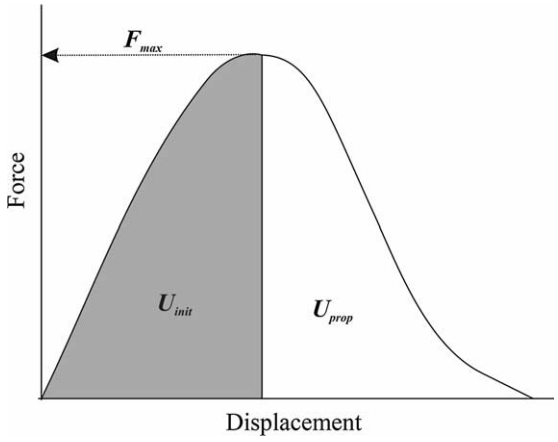

Fig. 3. Schematic of the force/displacement curve obtained during a CT test, illustrating quantities referred to in the text.

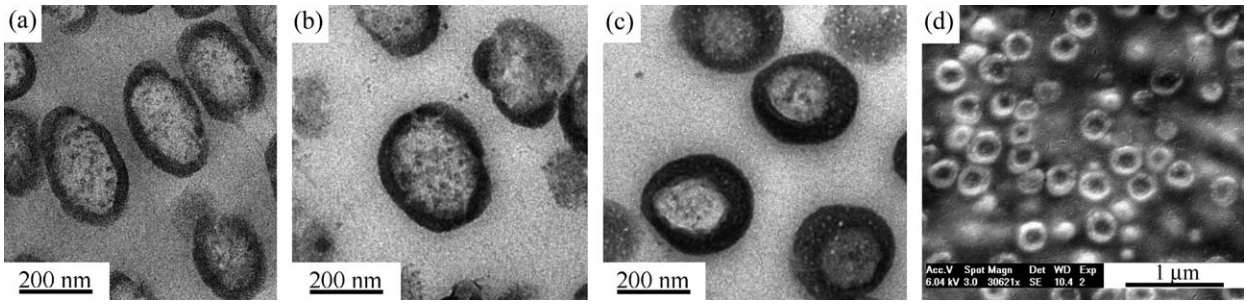

Fig. 4. TEM images of thin films of (a) V825-LC/3LA, (b) V825-HC/3LB and (c) V825-HC/3LC stained with RuO_4 and (d) SEM image of V825-HC/3LC stained with RuO_4.

inhomogeneous staining/sectioning and the presence of the copper grid may obscure certain parts of the crack tip zone, and low magnification imaging is less satisfactory).

To minimize relaxation of the crack tip damage zone in the deformed CT specimens, the crack faces were wedged open either while still under load, or, where the test speed was relatively high, immediately after testing [5,15]. In order to obtain a limited amount of stable crack growth at the highest speeds, two specimens were tested in series so that failure of one resulted in instantaneous unloading of the other, as described elsewhere [5]. The area around the crack tip was stained in order to provide sufficient contrast for SEM or TEM and to stabilize the specimen mechanically with respect to beam damage. This typically involved overnight exposure to RuO_4 vapor [7,16–18,20], which was able to diffuse into the crack tip deformation zone via the crack tip [10,19,21,22]. An internal surface from around the crack tip was then exposed using the ultramicrotome and gold coated for SEM observation and/or sectioned for TEM as described previously.

Deformation of films of sufficiently low thickness ($\leq$ 200 nm) for TEM observation in situ provided a convenient alternative to sectioning of bulk specimens. Sections of about 2×5 mm^2 in area were prepared by microtoming undeformed specimens of the various materials and floated onto distilled water, where they were exposed to chloroform vapor for a few minutes in order to relax any microtome induced damage. They were then picked up on annealed copper grids coated with a thin layer of the matrix polymer, to which they were bonded by a further short exposure to the solvent. After drying, the films were deformed in tension to a strain of about 10% along the grid diagonals at different speeds (from 1.7×10^{-6} to 1 m/s) using either a miniature tensile test machine (Minimat, Polymer Laboratories) or a simple falling weight apparatus for the highest speeds [23]. Plastic deformation of the copper grid maintained the films under tension after straining, so that individual grid squares could be observed by TEM without excessive relaxation of any deformation induced structure. RuO_4 staining was not used, because deformation in the form of cavitation or local necking generally resulted in adequate mass thickness contrast, provided the TEM images were recorded under low dose conditions, that is, conditions under which there was relatively little electron damage to the films, i.e. loss of detail and excessive specimen movement during observation.

3. Results

3.1. Dynamic torsion

Fig. 5 shows temperature sweeps of the loss modulus, G'', from dynamic torsion tests on $64\times12\times2$ mm^3 rectangular bars of the different matrices, obtained using a Rheometrics ARES (Advanced Rheometric Expansion System) at a constant frequency of 1 Hz and a maximum deformation of 0.1%. Consistent with the observed evolution of T_g (Table 1), T_α decreased with increasing comonomer content. On the other hand, the position of the main secondary relaxation peak corresponding to the rotation of methyl ester groups about the main chain axis [24], designated T_β in Fig. 5, was relatively insensitive to the comonomer content, so that $T_\alpha - T_\beta$ decreased from about 177 K in V825–LC to 90 K in V825–HC (Table 2). The strength of the β relaxation was nevertheless somewhat reduced in V825-HC. The influence of the particles on G'' is shown in Fig. 6, where the responses of V825-LC, V825-LC/3LB, V825-HC and V825-HC/3LC are compared. T_α was unchanged on particle addition, but the effective β

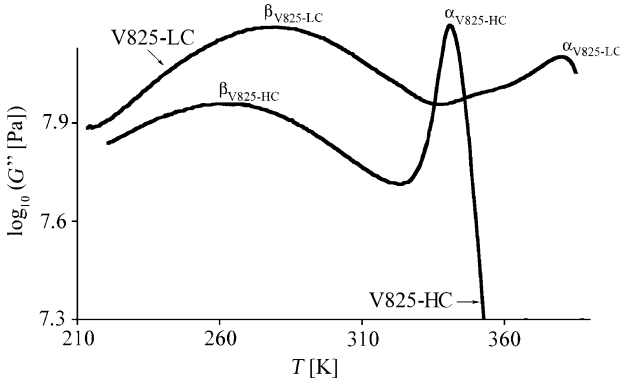

Fig. 5. G'' at 1 Hz from dynamic torsion measurements on the different matrices.

Table 2
T_α and T_β for the different matrices from dynamic torsion measurements at 1 Hz

	T_α (K)	T_β (K)	$T_\alpha - T_\beta$ (K)
V825-LC	397	280	117
V825-HC	353	263	90

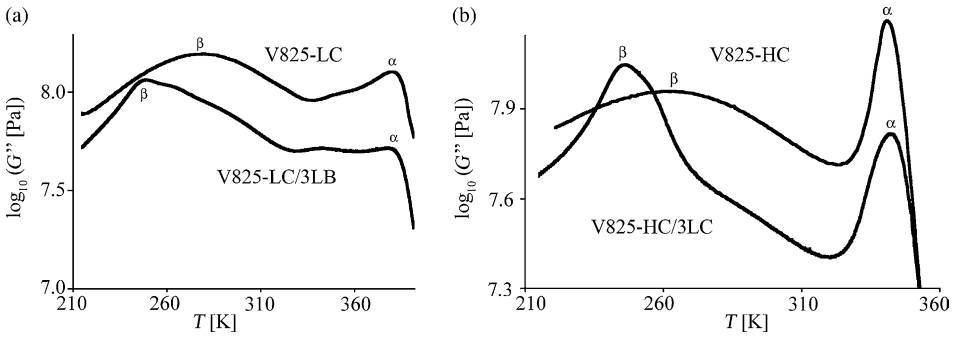

Fig. 6. G'' at 1 Hz from dynamic torsion measurements on (a) V825-LC and V825-LC/3LB, and (b) V825-HC and V825-HC/3LC.

transition was dominated by the glass transition of the rubbery phase of the particles (about 250 K in each case), which partly masked the β transition of the matrix.

3.2. Simple tensile tests

Representative stress-strain curves are given in Fig. 7 for V825-LC and V825-HC in simple tension, with and without particles and at different test speeds. At a test speed of 10^{-4} m/s, a high comonomer content led to a transition from brittle to ductile behavior in the matrix, as shown in Fig. 7(a), accompanied by a decrease in σ_y as defined in Section 2. Extensive yielding did not occur in the V825-LC under these conditions, whereas V825-HC showed a clear yield drop and ductile necking prior to failure. Particle addition to V825-LC also led to a marked increase in ductility at the same test speed, as shown in Fig. 7(b), with the 3LB particles giving a marginally lower σ_y and a significantly higher strain to break than the 3LA particles. Similar qualitative trends were observed on particle addition to V825-HC (Fig. 7(c)), but the absolute values of σ_y were consistently lower than those for the corresponding particle-toughened V825-LC grades. Results are also given in Fig. 7(c) for V825-HC/3LC, which showed nearly identical behavior to V825-HC/3LB. Increasing the test speed led to systematic increases in σ_y in all the materials and decreases in the strain to break, as illustrated by the stress–strain curves for V825-HC/3LC in Fig. 7(d). The evolution of σ_y with test speed was similar in all the materials, analysis in terms of the Ree-Eyring model for rate-activated yielding leading in each case to an activation volume close to the reported value of about 1 nm^3 for PMMA [25–27].

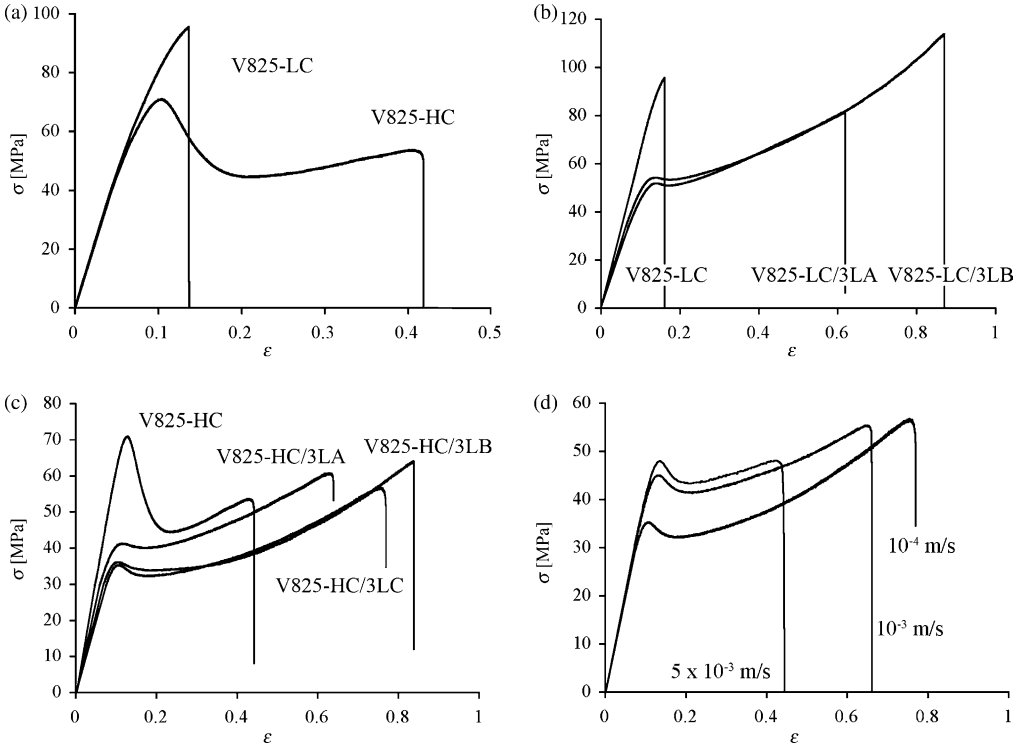

Fig. 7. Stress/strain curves in simple tension: (a) V825-LC and V825-HC at 10^{-4} m/s; (b) V825-LC, V825-LC/3LA and V825-LC/3LB at 10^{-4} m/s; (c) V825-HC, V825-HC/3LA, V825-HC/3LB and V825-HC/3LC at 10^{-4} m/s; (d) V825-HC/3LC at different test speeds.

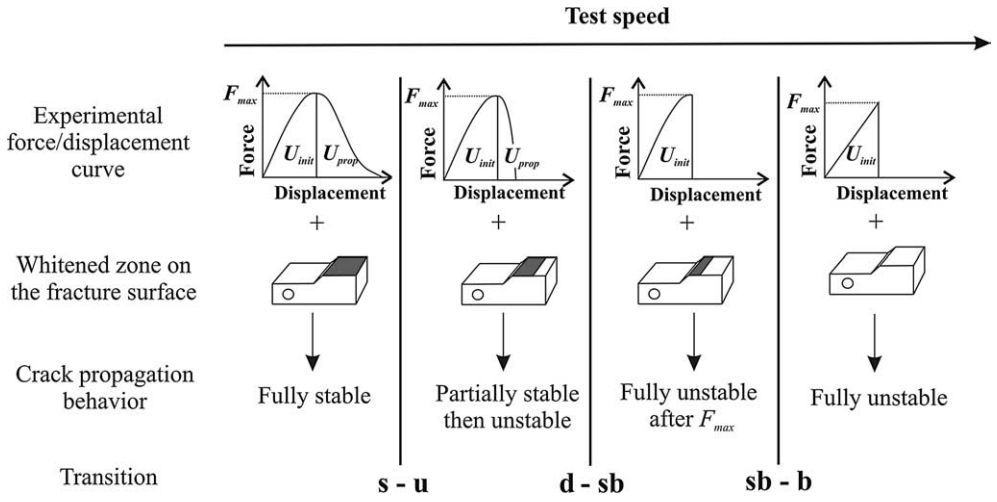

Fig. 8. Schematic representation of typical force/displacement curves in CT specimens showing the different regimes of behavior referred to in the text [22].

3.3. Fracture tests

Fig. 8 is a schematic representation of the force–displacement response in a CT specimen, based on previous observations of particle-toughened PMMA, which defines the various types of behavior to be referred to in what follows [5]. Transition s–u is a transition from stable to partly unstable behavior, generally with increasing test speed. At speeds below this transition, the fracture surface is strongly stress whitened in the particle-toughened grades. At higher speeds, stress whitening is only visible over part of the fracture surface, although the initial mode of fracture remains essentially ductile. Transition d–sb marks the onset of unstable failure for deformations immediately beyond the force maximum (semi-brittle behavior) and transition sb–b marks the onset of fully unstable failure at the force maximum (brittle behavior).

3.3.1. Matrix behavior

As shown in Fig. 9(a), the fracture behavior of V825-LC and V825-HC was broadly similar, and, although V825-HC showed a slightly higher crack initiation resistance (higher K_{max}) at high speeds, this trend was apparently reversed at low speeds. K_{max} was nevertheless relatively low in both matrices, reflecting their qualitatively fragile behavior, with unstable crack propagation being observed immediately beyond the force maximum ($U_{prop} \approx 0$). Fig. 10 shows the fracture surfaces for V825-LC and V825-HC (the notch and the pre-crack are on the left-hand side of each image). The V825-LC fracture surfaces were consistent with fully unstable crack propagation over the whole range of test speeds investigated, with no evidence of ductility even close to the crack tip. The V825-HC fracture surfaces were similar, but some roughness was visible along the crack path, assumed to be due to multiple crazing and/or crack bifurcation.

3.3.2. Particle-toughened materials

The particles had a marked effect on the fracture resistance of V825-LC, with K_{max} increasing by a factor of up to 2 over that of the matrix, as shown in Fig. 9(b). Crack propagation also became relatively stable, as reflected by U_{prop} (Fig. 9(c)). V825-LC/3LB showed better crack initiation resistance than V825-LC/3LA in that K_{max} was significantly increased over the whole range of test speeds, although U_{prop} was higher in V825-LC/3LA at high speeds. Fig. 10 shows the associated fracture surfaces. Stress whitening was visible over the whole of the fracture surfaces for V825-LC/3LA tested at 0.0001 and 0.001 m/s. At higher speeds, stress whitening remained widespread, but was less intense, although U_{prop} remained roughly constant and K_{max} even increased slightly in this regime, as shown in Fig. 9(b) and (c). Fracture surfaces for V825-LC/3LB tested at 0.0001 and 0.001 m/s, on the other hand, showed only partial stress whitening, and the behavior was, therefore, qualified as partly unstable. K_{max} and U_{prop} were nevertheless higher than for 3LA at these relatively low speeds (Fig. 9(b) and (c)). Full stress whitening and fully stable crack propagation were seen in V825-LC/3LB between 0.01 and 0.5 m/s, as for V825-LC/3LA, but at 1–9 m/s there was a transition to fully unstable crack propagation, associated with a marked decrease in U_{prop}.

Combining the more ductile matrix, V825-HC, with 3LA and 3LB particles also resulted in increased K_{max} with respect to that of the matrix over the whole range of test speeds, as shown in Fig. 9(d). As with V825-LC, the 3LB particles gave better reinforcement than the 3LA particles in terms of K_{max}, but they also gave very low U_{prop} at speeds greater than 0.1 m/s (Fig. 9(e)). The fracture surfaces for V825-HC/3LA at 0.0001 m/s (Fig. 10) showed intense stress whitening. At 0.001 m/s, the fracture surface was less regular, and, although the whitened zone remained extensive, a zone of unstable crack propagation corresponding to the final stages of fracture was also apparent, consistent with the drop in U_{prop} observed in this regime. Between 0.01 and 0.5 m/s, the fracture surfaces were less intensely stress whitened, but crack propagation was fully stable. Finally, at higher speeds, crack propagation was partly unstable, although K_{max} remained relatively high.

Crack propagation in V825-HC/3LB was more stable than in V825-LC/3LB at low speeds, as reflected by the extensive stress whitening of the corresponding fracture surfaces

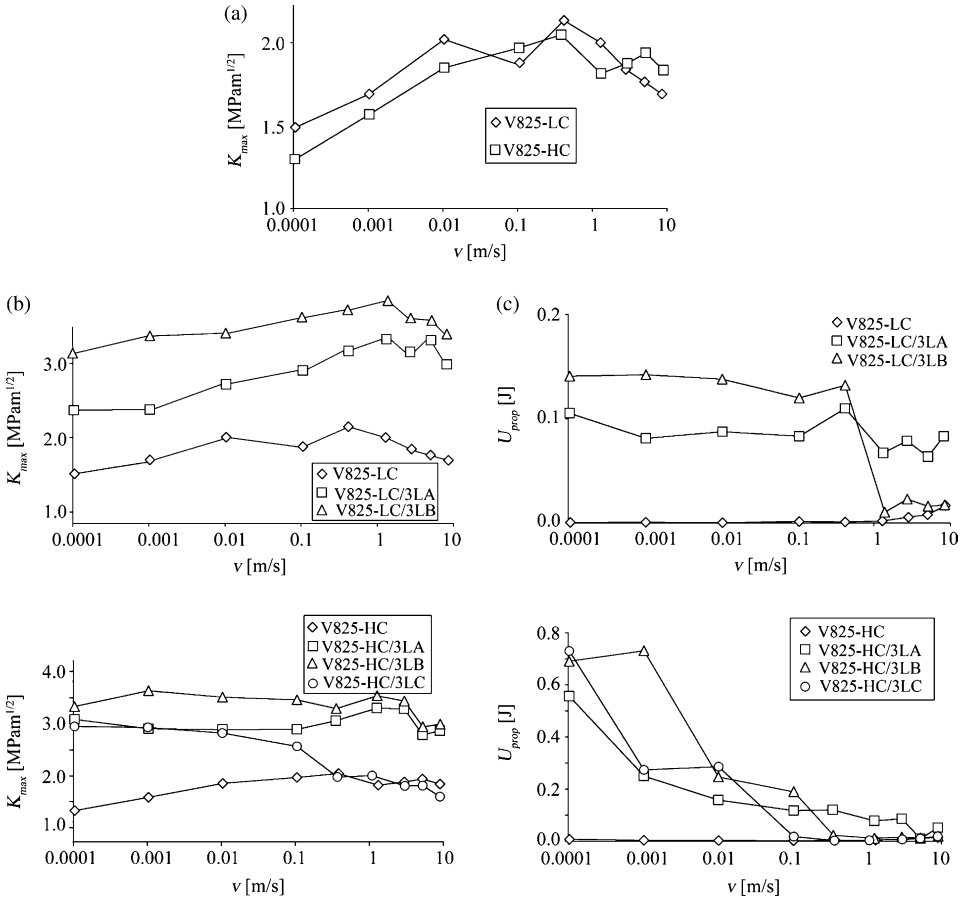

Fig. 9. (a) K_{max} for CT specimens of the different matrices as a function of test speed; (b) K_{max} for CT specimens of V825-LC and particle-toughened V825-LC as a function of test speed, (c) corresponding crack propagation energy; (d) K_{max} for CT specimens of V825-HC and particle-toughened V825-HC as a function of test speed and (e) corresponding crack propagation energy.

(Fig. 10), but became fully unstable above 0.1 m/s. Combining V825-HC with the 3LC particles also led to extensive stress whitening between 0.0001 and 0.01 m/s, and fully stable crack propagation. However, the performance was particularly poor at 0.1 m/s and above, where K_{max} and U_{prop} fell to values close to those obtained for the matrix (Fig. 10(d) and (e)), and crack propagation was already fully unstable.

K_{max} and U_{prop} are summarized in Fig. 11 for the 3LA and 3LB particle-toughened materials. The effect of a high comonomer content in specimens toughened with 3LA particles was generally to improve K_{max} and U_{prop} at low speeds. However, at high speeds (above about 0.1 m/s), U_{prop} and K_{max} were slightly reduced in V825-HC/3LA. In the case of the 3LB particles, the differences in K_{max} were less marked

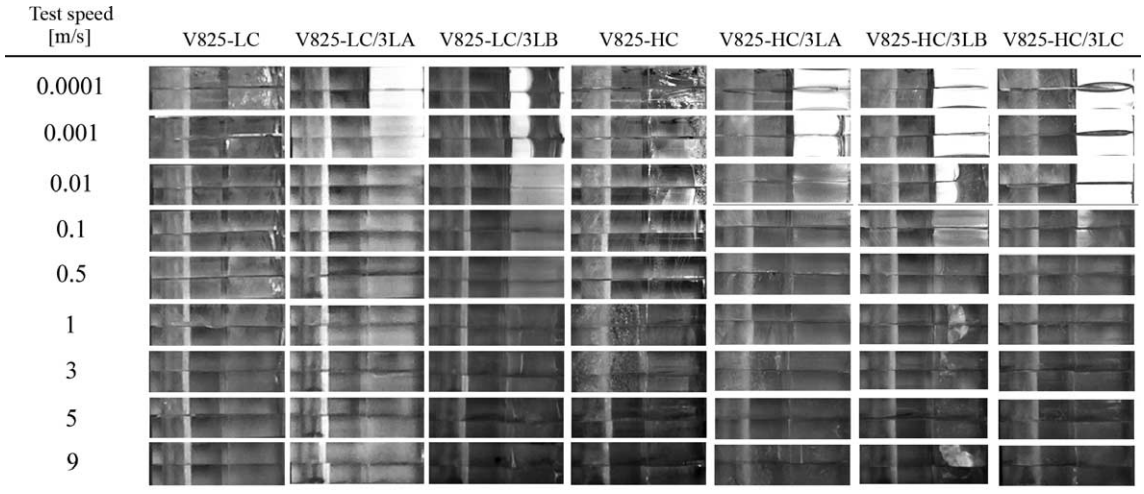

Fig. 10. Typical fracture surfaces from V825-LC, particle-toughened V825-LC, V825-HC and particle-toughened V825-HC CT specimens.

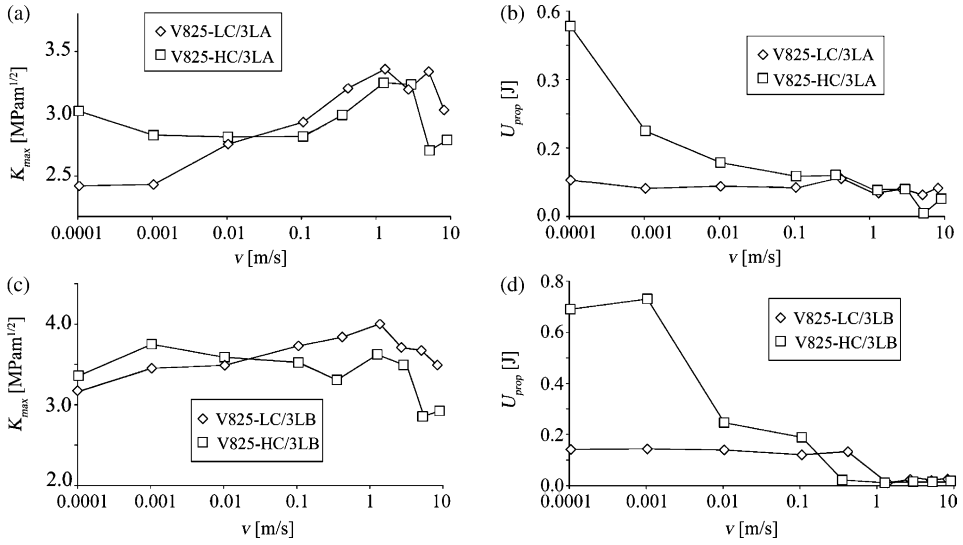

Fig. 11. (a) Maximum stress intensity factor for CT specimens of the different matrices toughened with 3LA particles; (b) crack propagation energy corresponding to (a); (c) maximum stress intensity factor for CT specimens of the different matrices toughened with 3LB particles; (d) crack propagation energy corresponding to (c).

at low speeds, but U_{prop} was again significantly greater in V825-HC/3LB than in V825-LC/3LB. At high speeds, K_{max} and U_{prop}, were also somewhat reduced in V825-HC/3LB. A systematic comparison was not made in the case of the 3LC particle-toughened grades.

3.4. Crack tip microdeformation mechanisms in the bulk

The SEM and TEM images in Figs. 12 and 13, respectively, show details from a relatively heavily stained flame-shaped region around the crack tip in a V825-LC/3LA CT specimen tested at 0.5 m/s, which represents the threshold of the high speed regime of fracture behavior. Well-defined bundles of crazes were apparent at the crack tip and also at the periphery of the stained region, and indeed TEM suggested crazing to be present throughout this region. Cavitation of the rubbery shells of the particles was also visible, and severe shear deformation in the immediate vicinity of the crack tip was inferred from the distortion of the particle cores. V825-HC/3LA deformed under the same conditions (Figs. 14 and 15) showed far more limited crazing (only visible in the TEM images), but shear deformation was again inferred to be present at the crack tip. Cavitation of the rubbery shells of the particles was evident throughout the stained region, which was about the same size as that in V825-LC/3LA. This is consistent with the observation of comparable K_{max} and U_{prop} in the two grades at 0.5 m/s, although the size of the stained region cannot be interpreted directly as a plastic zone size because it depends on the extent of RuO_4 penetration around the crack and hence on the percolation of cavitational deformation mechanisms such as crazing or cavitation of the particles. Indeed, optical images of semi-thin sections from the crack tip regions of the same specimens indicated some form of damage, tentatively identified with particle cavitation, to extend to up to 1–2 mm from the crack tip in both cases.

In V825-LC/3LA deformed in the low speed regime (10^{-4} m/s), some crazing was visible at the crack tip and in the wake of the crack, and particle cavitation remained evident. On the other hand, TEM images of the damage zone in V825-HC/3LA deformed at the same speed

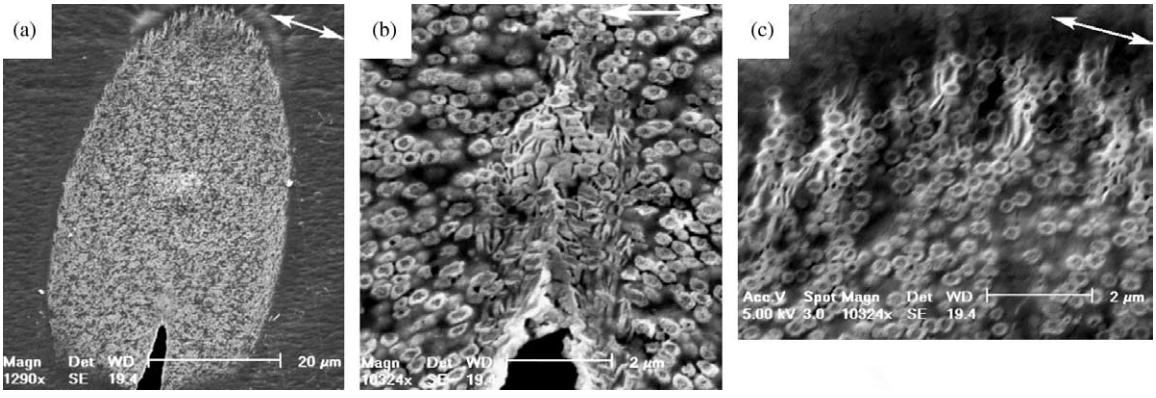

Fig. 12. SEM images of the crack tip zone of V825-LC/3LA deformed at 0.5 m/s, using the twin method to obtain crack arrest after a limited amount of propagation, and stained with RuO_4: (a) overview of the crack tip deformation zone; (b) crack tip; (c) periphery of the deformation zone.

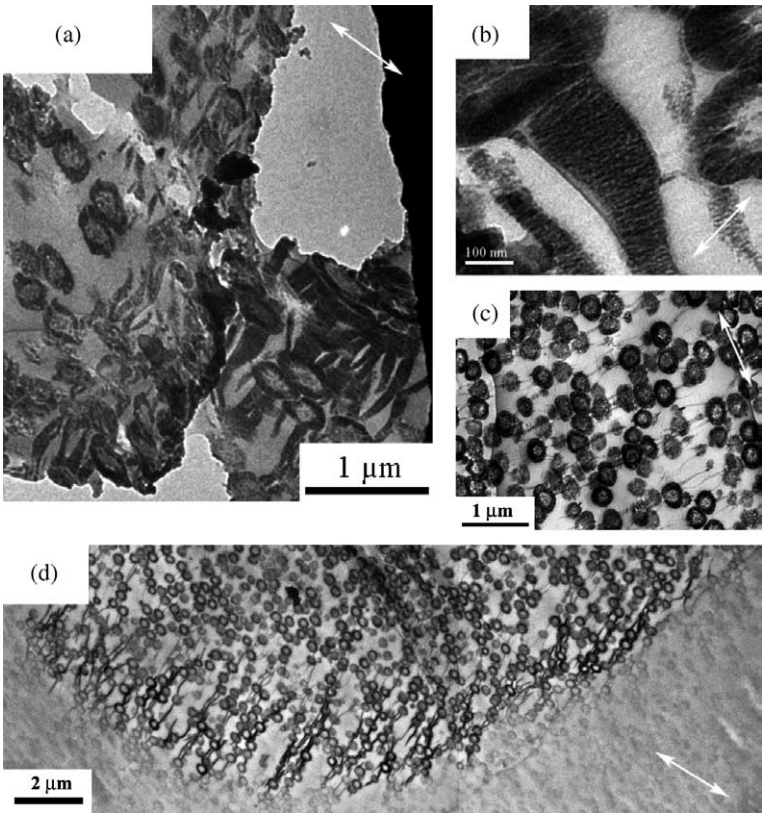

Fig. 13. TEM images of a thin section taken from the same specimen as in Fig. 12: (a) the crack tip; (b) detail of crazing/particle cavitation; (c) and (d) images from the periphery of the damage zone.

(Fig. 16) showed very little crazing. Particle cavitation was still visible, however, and shear deformation was also apparent around the crack tip. As shown in Fig. 17, the overall dimensions of the crack tip damage zone were very much greater in V825-HC/3LA than in V825-LC/3LA at 10^{-4} m/s, consistent with the greater K_{max} observed in V825-HC/3LA (Fig. 9).

3.5. Thin film deformation

Crazing was the dominant deformation mechanism in V825-LC thin films at intermediate test speeds. The corresponding TEM images (Fig. 18(a)) showed voids and fibrils within the deformed regions, although the structure of the craze interiors was often relatively homogeneous, an effect that has been attributed previously to fibril coalescence [11]. TEM observations of thin films of V825-HC suggested more widespread shear deformation (Fig. 18(b)). Homogeneous (non-fibrillar) deformation zones and shear bands whose trajectories were oriented with respect to the tensile axis coexisted with craze-like regions of higher extension ratio, but these latter did not show a well defined fibrillar structure. Such behavior is consistent with the more ductile tensile response seen in the bulk specimens of V825-HC, particularly at low speeds, where shear deformation

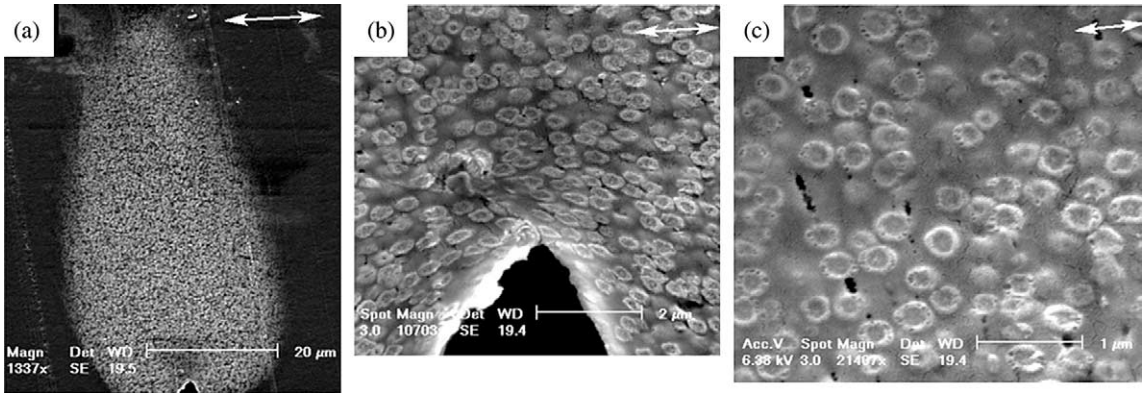

Fig. 14. SEM images of the crack tip zone of V825-HC/3LA deformed at 0.5 m/s, using the twin method to obtain crack arrest after a limited amount of propagation, and stained with RuO_4: (a) overview of the crack tip deformation zone; (b) crack tip; (c) periphery of the deformation zone.

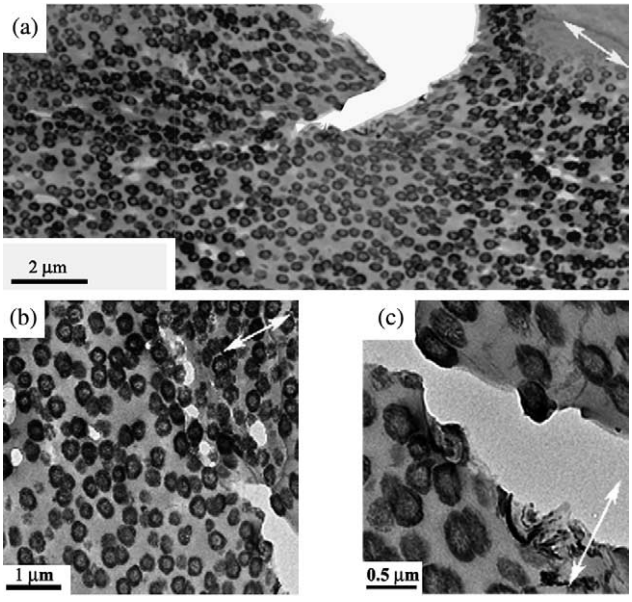

Fig. 15. TEM images of a thin section taken from the same specimen as in Fig. 14: (a) overview of the crack tip; (b) and (c) details from around the crack tip.

dominated in the thin films. Similarly, at high speeds, thin films of the matrices became qualitatively brittle, in that they tended to break down in the early stages of straining.

As shown in Fig. 19, the deformation speed also influenced the microdeformation mechanisms in thin films of the particle-toughened materials. In V825-LC/3LA tested at low speeds (1.7×10^{-6} and 1.7×10^{-5} m/s) a few short, wide crazes were visible in regions of the matrix between the particles, but the dominant deformation mechanism was extensive cavitation in the rubbery layers of the particles, leading to fibrillar deformation zones at the particle poles (with respect to the deformation axis) as has been described in detail elsewhere [7,28]. As the speed was increased to 1 m/s, however, more numerous, higher aspect ratio crazes appeared in the matrix and the extent of deformation of the particles diminished, with the implication that the particles were no longer as effective as 'craze stoppers'. Indeed, the micrograph in Fig. 19 suggests the craze trajectories to run through the particles themselves. The films also became qualitatively brittle under these conditions.

In V825-HC/3LA, extensive cavitation of the rubbery layers was observed at low speeds but crazing was largely absent, in accordance with the bulk observations (cf. Fig. 16). The main failure mode was the establishment of continuous paths of cavitated material associated with the rubbery shells of the particles, followed by homogenous deformation of the remaining matrix ligaments. At 1 m/s, however, V825-HC/3LA showed very similar behavior to V825-LC/3LA. Crazes with relatively high aspect ratios were clearly visible, with certain craze trajectories crossing individual particles, and the films were again qualitatively brittle. In V825-HC/3LB, cavitation and fibrillation of the rubbery layers of the particles were somewhat coarser than in V825-HC/3LA at all speeds, and crazing was less in evidence at 1 m/s, although the films remained relatively brittle.

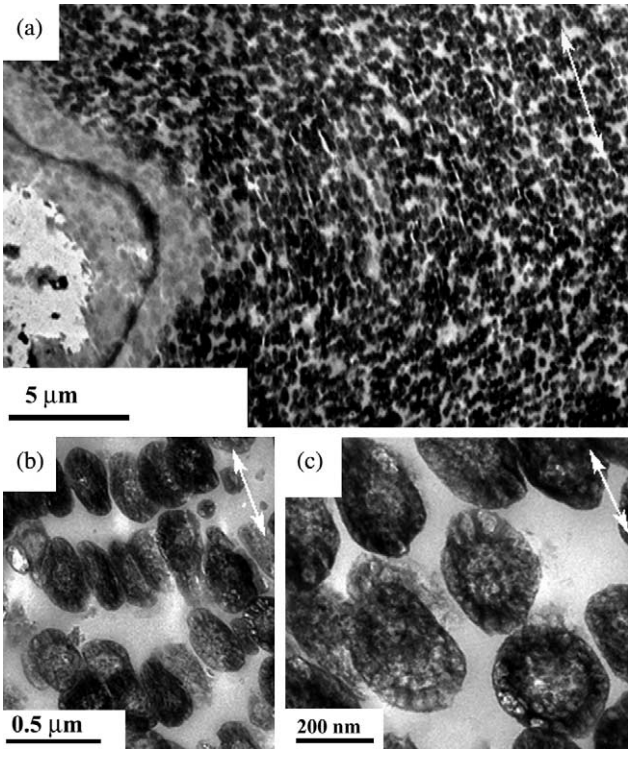

Fig. 16. TEM images of the crack tip damage zone of V825-HC/3LA deformed at 10^{-4} m/s using the twin method: (a) the crack tip; (b) and (c) details from around the crack tip.

4. Discussion

Given that increasing the comonomer content of the copolymers investigated here reduced T_g and M_e significantly, it follows from established models for the effect of the entanglement density, ν_e [29,30], that the resistance to crazing and hence the macroscopic ductility should improve. This was borne out in the present case by the behaviour in simple tension, and the trend towards increased ductility with increased comonomer content was confirmed in tests on copolymers with intermediate compositions. However, because of the proximity of T_β to room temperature in all the materials investigated, the β relaxation is also expected to play an important role in the strain rate sensitivity of the competing deformation mechanisms, namely simple shear and crazing, as has been discussed elsewhere for other types of copolymer, in which the strength and temperature of the β relaxation vary systematically [11]. Thus, although copolymers with intermediate comonomer contents were relatively ductile in simple tension at low strain rates, they became brittle as the strain rate increased within the limited range investigated. Indeed, in CT tests, where the triaxiality at the crack tip raised the effective yield stress, the behaviour of the copolymers remained brittle over the whole range of compositions and test speeds investigated, in spite of their improved ductility in simple tension. In the limiting case of a crack propagating through a single crack tip craze, which is to some extent justified in PMMA, the critical stress intensity factor K_C, may be shown to scale as $(DE/\sigma_c)^{1/2}\sigma_f$ [31], where E is the Young's modulus, D

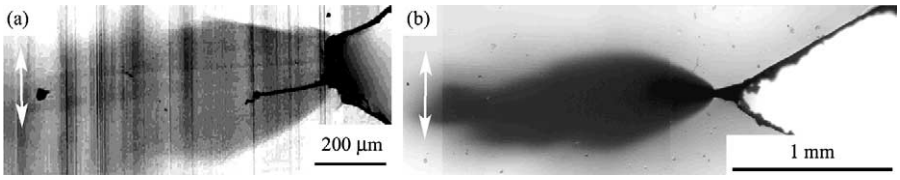

Fig. 17. Optical microscopy images of the damage zone in (a) V825-LC/3LA and (b) V825-HC/3LA, deformed at 10^{-4} m/s.

is the center-to-centre fibril spacing, σ_c is the stress at the craze interface and σ_f is the ultimate failure stress of a craze fibril. Assuming this to provide an indication of trends in K_{IC}, and given that the conditions for K_{IC} testing were generally met in the CT tests on the various matrices, it appears that any benefit from increasing ν_e by increasing the comonomer content (which will tend to increase σ_f) is offset by other factors such as increased σ_c or decreased stiffness (cf. Table 1). Proximity of the (constrained) yield stress to the crazing stress at high comonomer contents may explain the apparent trend towards multiple crazing and/or crack bifurcation seen at high speeds, but this again had little apparent effect on K_{IC}.

The effects of matrix modification on the mode I fracture response were far more marked in the particle-toughened materials tested at low speeds, with increased crack propagation resistance at high comonomer contents for all types of particle tested. Given the relatively high particle contents, cavitation of the particle cores was apparently sufficient to release constraints on local yielding without the need for extensive crazing, which has been argued to be necessary for constraint release at lower particle contents [7]. In the present case, low speed facture tets were generally occompanied by extensive particle cavitation at the crack tip and stable or partly unstable crack propagation, regardless of the particle type. There was some suggestion from the thin film tests that cavitation and the associated fibrillar structure linking the outer shell and the inner core in the 3LC particles after deformation, were relatively coarse. This may have been due to the increased thickness of the rubbery shell in these particles, and is thought to account for their poor performance at intermediate to high speeds. However, the most significant result from the thin film tests was that whereas crazing was absent in the particle-toughened films with high comonomer contents tested at low speeds, it was clearly present in all the grades tested at high speeds. This confirmed what was tentatively inferred from TEM of thin sections taken from the CT specimens: (i) at low speeds V825-LC/3LA and V825-LC/3LB showed crack tip crazing, but crazing was suppressed in V825-HC/3LA; (ii) crazing became more intense at crack tips deformed at higher speeds and was also present in V825-HC/3LA.

The onset of brittle behaviour in the rubber-toughened grades might be inferred on the above basis to be associated with a transition to crazing in all the matrices, regardless of the presence of the comonomer, and indeed similar behaviour was observed in specimens with intermediate comonomer contents. As mentioned previously, it may be significant in this respect that the β transition was relatively weakly influenced by the presence of the comonomer, the β transition's often being associated with temperature- or rate-induced transitions from shear to crazing [11,32]. However, the observation that the relatively long, high aspect crazes observed at high speeds in the thin films tended to pass through the particles without deviating suggested that it was the α transition of the rubbery layers (which coincided roughly with the matrix β transition) that limited performance in this regime. Rubber toughening can remain effective even in regimes dominated by crazing as borne out by the behaviour of the V825-LC based materials. On the other hand, if the rubber inclusions show increasingly glassy behaviour at high speeds, the stress concentrations that give rise to cavitation and/or delocalization of crack tip microdeformation at low speeds will no longer be effective. In view of the brittle behaviour of notched specimens of the unmodified matrices over the whole range of speeds investigated, the response of the rubber particles, therefore,

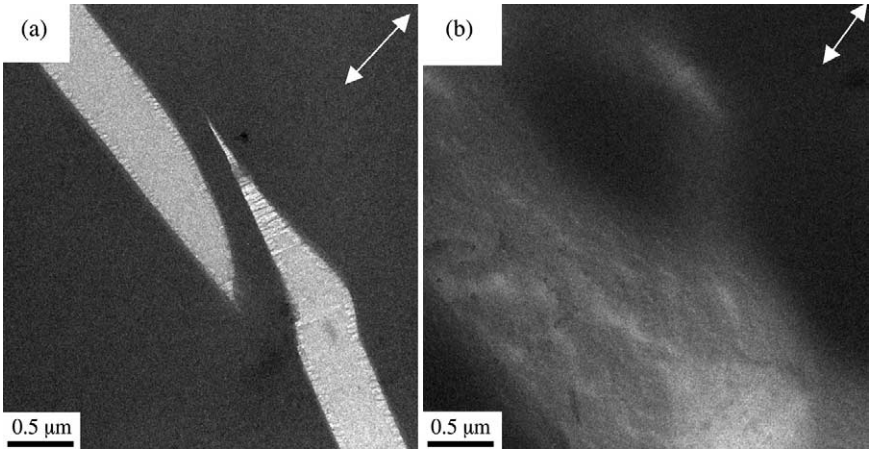

Fig. 18. TEM images of a thin film of (a) V825-LC and (b) V825-HC subjected to about 10% strain at 1.7×10^{-6} m/s.

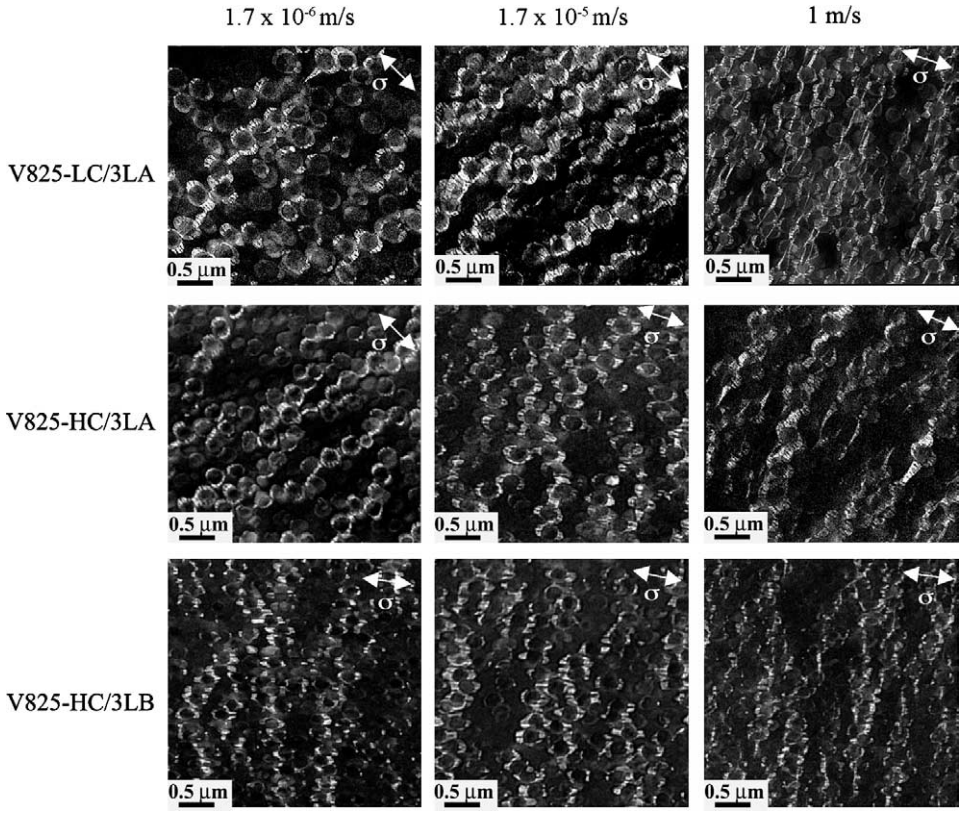

Fig. 19. Images of microtomed thin films of V825-LC/3LA, V825-HC/3LA and V825-HC/3LB deformed to 10% at different speeds.

limits the high speed performance in the present case, and synergistic effects are no longer possible.

5. Conclusion

It has been shown that increasing the comonomer content of PMMA-based copolymers decreases the transition temperatures corresponding to both the α and β relaxations, but that the α transition temperature, which corresponds to the glass transition, is more strongly reduced than the β relaxation temperature. The dominant room temperature deformation mode at low comonomer contents is crazing, whereas homogeneous shear deformation replaces crazing as the comonomer content increases and entanglement density decreases. The improved matrix ductility leads to increased crack propagation resistance in the particle-toughened grades at low speeds, without reducing K_{max}. On the other hand, the fracture performance diminishes significantly in all the grades at high speeds. This might be imputed to the transition from shear to crazing with increasing test speed observed in specimens with high comonomer contents. However, attenuation of the particle toughening effect at high speeds associated with the α transition of the rubbery phase is argued to limit fracture performance, regardless of the matrix microdeformation behavior. For the present series of particles, whose chemical composition and hence physical characteristics are constrained by the need to maintain good optical transparency, the advantages of matrix modification did not extend to high speeds if K_{max} or the crack propagation energy were used as toughness criteria. Improved performance of the toughening particles would, therefore, appear to be a prerequisite for the benefits of improved matrix ductility to be effective during mode I opening under impact conditions.

Acknowledgements

The authors would like to acknowledge the financial and technical support of Arkema and the technical support of the Centre Interdépartemental de Microscopie Electronique (CIME) of the EPFL.

References

[1] Lovell PA. Trends Polym Sci 1996;4:264–72.
[2] Lovell PA, Sherratt MM, Young RJ. Toughened plastics II. Novel approaches in science and engineering. In: Riew CK, Kinlock AJ, editors. ACS advances in chemistry series, vol. 252; 1996, 1996. p. 211–32.
[3] Adams JM. Clay Miner 1993;28:509–30.
[4] Nguyen G, Matlengiewicz M, Nicole D. Polish J Chem 2003;77:447–58.
[5] Béguelin P. PhD Thesis. Ecole Polytechnique Fédérale de Lausanne; 1996.
[6] Tang H, Martin DC. J Mater Sci 2003;38:803–15.
[7] Plummer CJG, Béguelin P, Kausch H-H. Colloids Surf, A—Physicochem Eng Aspects 1999;153:551–66.
[8] Lach R, Adhikari R, Weidisch R, Huy TA, Michler GH, Grellmann W, et al. J Mater Sci 2004;39:1283–95.
[9] Fond C, Schirrer R. CR Acad Sci, Ser II Fascicule B—Mécanique 2001; 329:195–200.
[10] Lauterwasser BD, Kramer EJ. Philos Mag A—Phys Condens Matter Struct Defects Mech Prop 1979;39:469–95.

[11] Plummer CJG, Kausch H-H, Tézé L, Halary JL, Monnérie L. Polymer 1996;37:4299–305.
[12] Groupement De Recherche De Lacq, Personal communication; 2002.
[13] Moore DR, Pavan A, Williams JG. Fracture mechanics testing methods for polymers, adhesives and composites. New York: European Structural Integrity Society; 2001.
[14] Béguelin P, Kausch H-H. J Phys IV 1997;7:933–8.
[15] Plummer CJG, Mauger M, Béguelin P, Orange G, Varlet J. Polymer 2004; 45:1147–57.
[16] Adla A, Buschmann V, Fuess H, Trautmann C. Nucl Instrum Methods Phys Res Sect B—Beam Interact Mater 2001;185:210–5.
[17] Trent JS, Scheinbeim JI, Couchman PR. Macromolecules 1983;16: 589–98.
[18] Vitali R, Montani E. Polymer 1980;21:1220.
[19] Okamoto M, Shinoda Y, Kojima T, Inoue T. Polymer 1993;34:4868–73.
[20] Adla A, Fuess H, Trautmann C. J Polym Sci, B—Polym Phys 2003;41: 2739–50.
[21] Plummer CJG, Beguelin P, Grein C, Gensler R, Dupuits L, Gaillard C, et al. Macromol Symp 2004;214:97–114.
[22] Béguelin P, Plummer CJG, Kaush HH. In: Shonaike GO, Simon GP, editors. Polymer blends and alloys. New York: Marcel Dekker; 1999. p. 549–73.
[23] Plummer CJG, Béguelin P, Kaush HH. Polym Eng Sci 1995;35:1300–12.
[24] Bartenev GM, Lomovskoi VA, Ovchinnikov EY, Karandashova NY, Tulinova V. Vysokomolekulyarnyne Soedineniya Seriya A, Seriya B 1993;35:1659–68.
[25] Richeton J, Ahzi S, Daridon L, Remond Y. J Phys IV 2003;110:39–44.
[26] Klompen ETJ, Govaert LE. Mech Time-Depend Mater 1999;3:49–69.
[27] Kausch HH, Heymans N, Plummer CJG, Decroly P. Traité Des Matériaux 14—Matériaux Polymères: Propriétés Mécaniques et Physiques. Lausanne: Presses Polytechniques et Universitaires Romandes; 2001.
[28] Michler GH. J Macromol Sci, Phys 2001;B40:277–96.
[29] Henkee CS, Kramer EJ. J Mater Sci 1986;21:1398–404.
[30] Kramer EJ. Adv Polym Sci 1983;52:1–56.
[31] Bubeck RA, Buckley DJ, Kramer EJ, Brown HR. J Mater Sci 1991;26: 6249–59.
[32] Kausch H-H, Halary JL, Plummer CJG. Macromol Symp 2004;214: 17–30.